AERODYNAMIC INTERACTIONS BETWEEN A HELICOPTER ROTOR AND A T-TAIL EMPENNAGE

J. Gordon Leishman* Erwin Moedersheim†

Center for Rotorcraft Education and Research
Department of Aerospace Engineering
Glenn L. Martin Institute of Technology
University of Maryland at College Park

Abstract

Experiments were conducted to study the aerodynamic interactions between a small-scale helicopter rotor and a T-tail type empennage. Time-averaged and unsteady pressure measurements were made at various chordwise and spanwise stations on a horizontal tailplane. Flow visualization was performed using the wide-field shadowgraph method to help identify the locations of the rotor tip vortices relative to the empennage, and supported the interpretations of the surface pressure responses. The results have shown that the tailplane operated in a highly unsteady environment, with large spanwise and chordwise variations in aerodynamic loading. The proximity of the rotor wake boundary was found to be a fundamental factor influencing the flow environment at the tailplane.

Nomenclature

b	Span of horizontal tailplane, m
c	Chord of horizontal tailplane, m
c_b	Rotor blade chord, m
C_l	Lift coefficient
C_{p_0}	Total pressure coefficient, $= (p_0 - p_\infty) / (p_{0_\infty} - p_\infty)$
C_p^u	Time-dependent pressure coefficient, $= 100\ (p(t) - p_\infty) / 0.5\rho\Omega^2 R^2$
C_p'	Time-averaged pressure coefficient, $= 100\ (p - p_\infty) / 0.5\rho\Omega^2 R^2$
C_T	Rotor thrust coefficient, $= T/\rho\pi\Omega^2 R^4$
k	Reduced frequency
N_b	Number of blades
R	Rotor radius, m
T	Rotor thrust, N
V_∞	Free-stream velocity, m/s
V_y	Lateral velocity component, m/s
V_z	Vertical velocity component, m/s
x_h, y_h, z_h	Hub coordinate system, m
x, y, z	Tailplane coordinate system, m
α_s	Shaft angle, $deg.$
μ	Advance ratio, $=V_\infty/\Omega R$
ρ	Air density, kg/m^3
σ	Rotor solidity, $= N_b\ c_b/\pi R$
ψ	Blade azimuth angle, $deg.$
Ω	Rotor rotational frequency, rad/s

*Associate Professor.

†Graduate Research Assistant.

Presented at the 22nd European Rotorcraft Forum, 17-19 Sept. 1996, Brighton, UK.

Introduction

All rotorcraft suffer from interactional aerodynamic problems whereby the rotor affects the airframe airloads and the airframe has a reciprocal affect on the rotor airloads and performance. Interactional aerodynamic effects are always accentuated by the use of high rotor disk loadings and smaller clearances between the main rotor and the fuselage. However, the mechanisms contributing to these aerodynamic interactions are complicated, and as of yet are not fully understood. Yet it is known that the energetic wake generated by the rotor may envelope large parts of the airframe, thereby affecting the airloads in these regions.[1, 2] Furthermore, the strong tip vortices generated by each rotor blade may come in close proximity to or impinge the airframe surface, and this can be a source of large unsteady airloads.[3, 4]

While there have been many rotor/airframe interaction studies, systematic experimental studies of helicopter rotor/empennage interactions are rare. The consequences of the problem, however, can be very signficant. During changes in forward flight speed the rotor wake boundary changes position significantly relative to the empennage, which means that large excursions in angle of attack can occur there. Combined with the high total pressure inside the rotor wake boundary, this can result in substantial changes to fuselage forces and moments. If these changes occur suddenly or unpredictably, then an aircraft with undesirable handling qualities can result. The difficulties with the horizontal tailplane design on the AH-64 Apache and EH-101 helicopters are documented examples of this type of problem.[5, 6] In addition, because of the large unsteady effects associated with the rotor wake/surface interactions, vibration levels can be significantly amplified when the interactions take place at the end of a long tail.

Early investigations into rotor/surface interaction problems include the work of Wheatly,[7] Makofski and Menkick,[8] McKee and Naeseth[9] and Lynn.[10] Sheridan and Smith[11] examined some of the more detailed issues associated with rotor/tail airloads in their seminal work on rotor/airframe interactions. More recently Leishman and Bi[12] studied the interactions between a rotor and an isolated lifting surface, confirming the complexity of the aerodynamic problem. Because of high vibrations found on the RAH-66 T-tail configuration, Torok and Ream[13] obtained flight test data documenting the interactions and attempted to understand their source. Frederickson and Lamb[14] conducted a further investigation in a wind tunnel test of the RAH-66 Comanche. In both tests, the vibration levels produced by the rotor/tail interactions were clearly correlated with the wake position.

The theoretical prediction of the effects of rotors and the associated vortical wakes on the airloads induced airframe components has also received some attention. Bramwell[15] has used potential flow methods with simple configurations, and the significance of unsteady effects was clearly demonstrated. Yet the development of higher fidelity methods has been hindered by the lack of detailed experimental data, both for guidance in developing the models and for validation purposes. Gangwani[16, 17] used a prescribed wake model coupled with a doublet-lattice model of a fixed wing to predict the unsteady bending moments measured on a helicopter tail. Reasonable correlation was obtained with flight test data. Mello and Rand[18] confirmed that the predicted unsteady loads on the empennage were very sensitive to the rotor wake geometry. Curtiss and Quackenbush[19] considered the effects of the rotor wake induced velocity field at the empennage location on helicopter stability derivatives. The limited correlations obtained with flight test data reiterated the complexity of the wake/empennage interaction problem. Recently, Weinstock[20] has developed a simple model of the aerodynamic interaction problem for use in flight simulation modeling.

In view of the present limited understanding of the very complicated and interrelated effects of rotor/empennage aerodynamic interactions, the purpose of the present work was to conduct a systematic experimental investigation into the problem. Particular emphasis was placed on documenting the rotor wake geometry and unsteady effects induced on a horizontail tail. The overall objective was to obtain a better understanding of the aerodynamic environment encountered by lifting surfaces located near a rotor and/or immersed in the rotor wake, and to provide specific measurements for ongoing validation studies with analytical models.

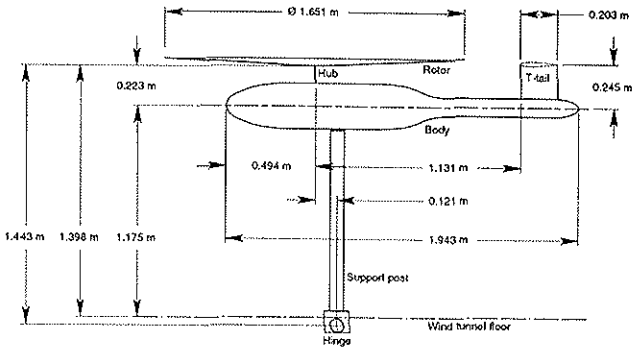

Figure 1: Sketch of the rotor/body/empennage system, high tailplane position

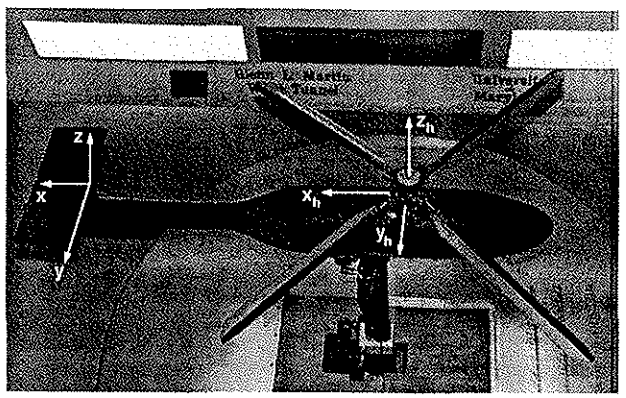

Figure 2: Photograph of the rotor/body/empennage system in the wind tunnel

Description of the Experiment

The experimental set-up consisted of a an approximately 1/6-scale four-bladed helicopter rotor and generic body shape. This set-up has been used for many years for several different studies at the University of Maryland,[1–3] and is an AGARD test case for rotor/airframe interaction modeling.[21] The rotor has a fully articulated hub with four blades and a conventional swashplate. The rotor diameter is $1.65\,m$ ($65\,in$). The blades used were mildly tapered in planform with a taper ratio of 3:1 confined to the outermost 6% of the blade. The blades had 13 degrees of nose-down linear twist. In the present experiments a T-tail empennage was located on the generic body shape $1.131\,m$ ($44.5\,in$) downstream of the rotor hub, as illustrated in Fig. 1. The tailplane was supported by a structure inside the tailboom, which for some tests contained a strain-gage balance.

The T tail empennage configuration comprised a horizontal tailplane with a constant chord of $0.203\,m$ ($8.0\,in$), connected to the tail by an aerodynamic fairing of the same chord. The aspect ratio of the tailplane was 2.5. Both the horizontal and vertical tail employed a NACA 0012 airfoil throughout. The horizontal tailplane could be located at two vertical positions, namely $z_h/R = +0.022$ (high tailplane configuration) and $z_h/R = -0.055$ (low tailplane configuration). These configurations simulated most of the aerodynamic conditions likely to be encountered by a horizontal tailplane on a typical helicopter. The tailplane was mounted at zero degrees angle of attack relative to the longitudinal axis of the body.

A summary of the main characteristics of the rotor, fuselage, and tail assembly is given in Table 1, with a photograph of the setup being shown in Fig. 2. This photograph also illustrates the two coordinate systems.

Rotor and Tailplane Instrumentation

Instrumentation was installed on the rotor and the empennage. Instrumentation was not provided on the body in these particular tests because it had been extensively instrumented in a previous series of tests.[2–4] The rotor balance permitted the measurement of three mutually perpendicular time-averaged force components (thrust, drag, and side-force), along with the corresponding moments. Rotor power was measured using a torque disk coupled to the rotor shaft. Hall-effect sensors were located at the blade hinges to monitor flap and lead/lag displacements. Details of other rotor instrumentation are given in Ref. 3.

Time-averaged pressure measurements were obtained from thirty-two pressure taps. These were located along rows at the leading-edge at $x/c = 0.04$ and the trailing-edge at $x/c = 0.81$ on both the upper and lower surface of the tailplane – see Table 2. The

Number of blades, N_b	4
Rotor radius, R	$0.826\,m$ $(32.5\,in)$
Rotor blade chord, c_b	$63.5\,mm$ $(2.5\,in)$
Rotor solidity, σ	0.098
Blade twist (linear)	$-13°$
Blade airfoil	NASA RC310/410
Fuselage length	$1.943\,m$ $(76.5\,in)$
Fuselage max. diameter	$0.254\,m$ $(10.0\,in)$
Tailplane span, b	$0.508\,m$ $(20.0\,in)$
Tailplane chord, c	$0.203\,m$ $(8.0\,in)$
Tailplane airfoil section	NACA 0012
High tailplane position, z_h/R	+0.022
Low tailplane position, z_h/R	−0.055

Table 1: Main geometric characteristics of the rotor, fuselage and tail models

Pressure Tap No.			
Top	Bottom	x/c	$2y/b$
1	17	0.04	0.80
2	18	0.04	0.60
3	19	0.04	0.40
4	20	0.04	0.20
5	21	0.04	-0.20
6	22	0.04	-0.40
7	23	0.04	-0.60
8	24	0.04	-0.80
9	25	0.81	0.80
10	26	0.81	0.60
11	27	0.81	0.40
12	28	0.81	0.20
13	29	0.81	-0.20
14	30	0.81	-0.40
15	31	0.81	-0.60
16	32	0.81	-0.80

Table 2: Locations of static pressure taps on the horizontal tailplane

leading-edge pressure taps were positioned to detect the leading-edge pressure peak, and therefore, to give an indication of the local lift coefficient of the tailplane section. When correlated with the leading-edge pressure response, the trailing-edge pressures helped indicate the occurence of flow separation. The pressures were measured using a digital multi-channel pressure system. The pressure tubes were connected to a multiplexer module mounted inside the fuselage. This module contained miniature pressure transducers, analog multiplexers, and analog-to-digital (A/D) converters. A miniature pneumatic valving system inside the module permitted rapid on-line recalibration of the pressure sensors with the test in progress.

Time-dependent pressures were measured using pressure transducers located at sixteen locations, and grouped at two spanwise stations — see Table 3. Due to physical constraints, it was impractical to co-locate the pressure transducers at the same chordwise or spanwise locations as the static pressure taps, so they were offset by a small distance.

Transducer No.			
Top	Bottom	x/c	$2y/b$
1	9	0.075	0.50
2	10	0.263	0.50
3	11	0.494	0.50
4	12	0.725	0.50
5	13	0.075	-0.50
6	14	0.263	-0.50
7	15	0.494	-0.50
8	16	0.725	-0.50

Table 3: Locations of pressure transducers on the horizontal tailplane

Data Acquisition System

Time-averaged pressure data were acquired from the pressure measuring system over a GPIB interface. Quasi-steady data, such as rotor balance loads, were logged directly by a computer through a 16-channel multiplexer and a 14-bit A/D converter. Unsteady pressure data were logged simultaneously using a high-speed multi-channel 12-bit A/D converter system. This data acquisition system was also interfaced over a GPIB interface. A trigger signal for all the unsteady measurements was obtained from a rotor shaft encoder.

The time-averaged pressure measurements were made by averaging 256 samples at each location over an interval corresponding to about 200 rotor revolutions. Time-histories of the pressure transducer responses were logged continuously over up to 20 rotor revolutions at a sampling resolution of 256 data frames per channel per revolution, i.e., an azimuth resolution of 1.4 *deg*. All unsteady time-history data presented in this paper are time-averaged, i.e., the data were ensemble averaged over ten or more rotor revolutions.

Test Conditions

The experiments were performed in the University of Maryland's Glenn L. Martin wind tunnel. This tunnel has a $2.36 \times 3.35\,m$ $(8 \times 11\,ft)$ working section. The rotor was tested at a rotational speed of $2100\,rpm$ $(35\,Hz)$, which corresponded to a nominal hover tip Mach number of 0.52. Collective, lateral cyclic and longitudinal cyclic blade pitch were set by means of remotely controlled swashplate actuators. The normal forward flight trim procedure was performed by minimizing the 1-per-revolution blade flapping response relative to the shaft, thereby producing a rotor tip-path-plane (TPP) that was perpendicular to the rotor shaft axis.

Over seventy test conditions comprising variations in rotor thrust, advance ratio, shaft angle, and tailplane position were examined; the range of test parameters being summarized in Table 4. Comparative studies were conducted at a constant rotor thrust for different advance ratios and shaft tilt angles. The results shown in this paper are mostly for a blade loading coefficient of $C_T/\sigma = 0.075$.

Parameter	Test Values
Advance ratio, μ	0.05 to 0.30
Rotor shaft angle, α_s	$-6°$ to $+4°$
Rotor rotational speed	$2100\,rpm$ $(35\,Hz)$
Rotor hover tip Mach no.	0.52
Blade loading, C_T/σ	0.075, 0.080, 0.085

Table 4: Range of test parameters

Flowfield Survey

Flowfield survey data, which were origionally obtained by Leishman and Bi[21, 22] were reanalysed and used as a reference for the current tests. The time-averaged total pressure and three components of velocity were measured by miniature seven-hole probes. These data were obtained during a test with the same rotor, both with and without the body. Data at three advance ratios (μ = 0.075, 0.10, and 0.20) were measured at a blade loading of C_T/σ = 0.075. The probes were mounted on a traversing rig and were moved in three horizontal planes located at $z_h/R = -0.14, -0.29$, and -0.45. While these planes were somewhat below the plane of the horizontal tailplane used in the present test, the data provided considerable information about the flow environment at the tail. The measurement grid contained 896 measurement points (28×32 grid) in each plane, mostly equispaced at $7.62\,cm$ $(3.0\,in)$.

Flow Visualization

The wide-field shadowgraph technique was used to visualize the locations of the rotor tip vortices relative to the empennage. The basic components of the shadowgraph system are a point light source strobe, a retroreflective projection screen, and a video or still camera. The tip vortices created by the rotor cause small changes in the flow density and index of refraction. Therefore, the light rays from the strobe are refracted as they pass through these vortices, causing (magnified) shadows to be cast on the projection screen. By examining the wake for successive rotor azimuth positions and by using a grid system on the screen, it was possible to quantify the locations of the leading- and trailing-edges of the rotor wake boundary relative to the rotor and the empennage. Further details of the wide-field shadowgraph technique can be found in Ref. 23.

Results and Discussion

Flowfield Measurements

The distribution of total pressure at the highest measurement plane is illustrated in Fig. 3. The relative position of the rotor disk and the tailplane are also provided on the figure for reference.

The highest total pressures were found to occur near the periphery of the rotor disk. Note that this is more pronounced on the retreating side, since the lift tends to be concentrated more toward the tip on this side of the rotor disk. A small low pressure region can be observed in Fig. 3 on the advancing side just behind the center of the rotor disk. This is due to the presence of the hub wake, which appears on this side

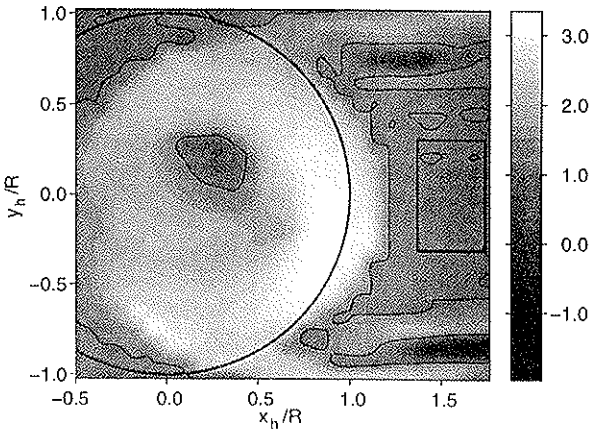

Figure 3: Distribution of C_{p_0} at $z_h/R = -0.14$ for $\mu = 0.10$ (isolated rotor)

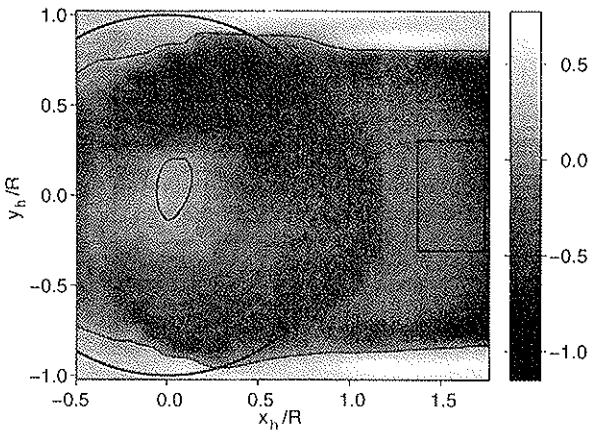

Figure 4: Distribution of vertical velocity V_z/V_∞ at $z_h/R = -0.14$ for $\mu = 0.10$ (isolated rotor)

of the disk due to the (small) swirl flow in the direction of rotor rotation. This hub wake was found to be convected further downstream as the advance ratio was increased, but at no time did it impinge on the empennage region. Previous research[11, 24] has shown that the rotor hub wake can have a considerable influence on the flow environment of the empennage at high advance ratios. However, for the measurements made here, which were for advance ratios of 0.3 and below, the hub wake was convected below the empennage. This was also evident from the flow visualization, which showed that the tip vortices passing near the tailplane were not affected by turbulence generated by the hub wake.

The region behind the rotor disk, which is where a horizontal tailplane may be located on a helicopter, was characterized by fairly low total pressure. However, the individual velocity components revealed that there was a significant downflow at this position. This is illustrated by Fig. 4, which shows the contours of the vertical component of measured velocity V_z (nondimensionalized with respect to the free-stream velocity). The two low pressure regions trailing from the edges of the rotor disk in Fig. 3 provided evidence of the wake roll-up into two larger vortex bundles. Examination of the V_z component in Fig. 4 shows the

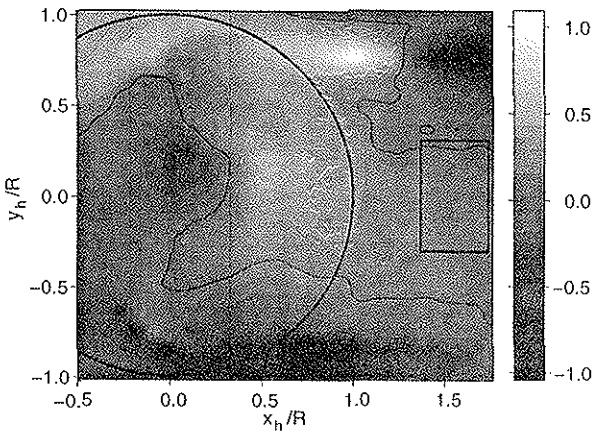

Figure 5: Distribution of lateral velocity V_y/V_∞ at $z_h/R = -0.14$ for $\mu = 0.10$ (isolated rotor)

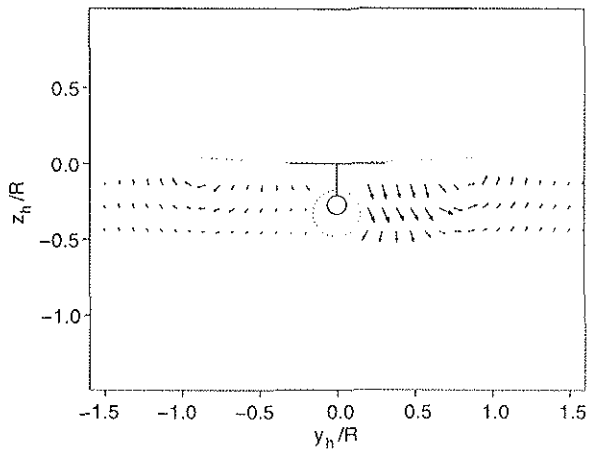

Figure 6: Velocity distribution in yz-plane at $x_h/R = 1.28$ for $\mu = 0.10$ (isolated rotor)

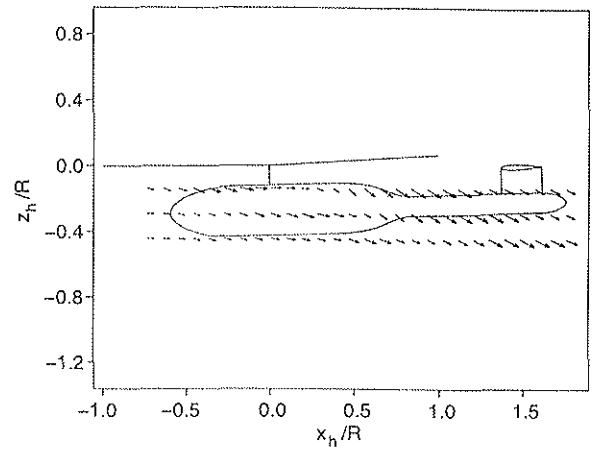

Figure 7: Velocity distribution in xz-plane at $y_h/R = 0.20$ for $\mu = 0.10$ (isolated rotor)

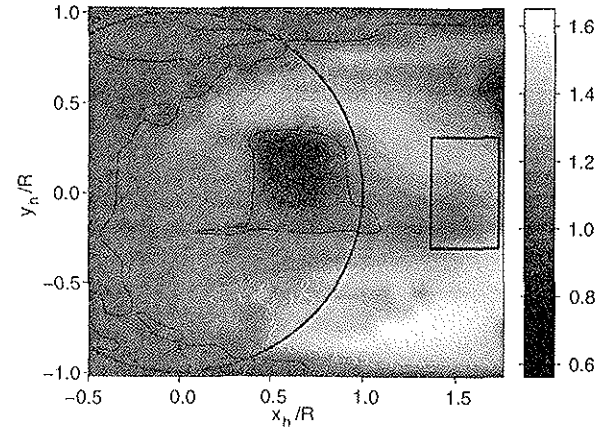

Figure 8: Distribution of C_{p_0} at $z_h/R = -0.14$ for $\mu = 0.20$ (isolated rotor)

presence of these vortex bundles, with large positive and negative velocity peaks occurring when the vortex bundles were close to the measurement plane. This is particularly visible near $y_h/R = \pm 0.80$ just behind the rotor disk. Also note that the flowfield was not fully symmetric. In general, the V_z velocity peaks and gradients on the advancing side were larger suggesting that the trailing vortex bundle on the advancing side was stronger. This was also observed in another rotor experiment by Ghee and Elliott.[25]

Figure 5 shows the distribution of the non-dimensional lateral velocity V_y, again illustrating the significant asymmetry of the flowfield near the empennage location. As with the V_z component the effect induced by the tip vortex bundles was larger on the advancing side of the disk, which is visible at $x_h/R = 1.28$ and $y_h/R = 0.80$. In general, the flow direction between the vortex bundles was oriented towards the centerline of the body when the measurement plane was above the vortex plane, and away from the centerline when the measurement plane was below the vortex plane.

The lateral and vertical velocity components have been combined in Fig. 6 to give another impression of the velocity field induced by the rotor wake. In this plot, the flowfield is shown for a cross-plane at $x_h/R = 1.58$, which is approximately equivalent to the 11% chord location in the tailplane coordinate system. The position of both vortex bundles trailed from the rotor disk can be determined without much difficulty. It is noteworthy that the vortex bundle on the advancing blade side was convected further down below the rotor at this cross-plane, a phenomenon that was also observed by Ghee and Elliott.[25]

Figure 7 shows the development of the wake velocities in a longitudinal plane at $y_h/R = 0.20$, just to starboard of the body centerline. In the vicinity of the horizontal tailplane (which is just downstream of the wake boundary at this advance ratio) the velocities decreased considerably (as illustrated previously by the total pressure measurements) but the downwash angles still remained quite large. Therefore, it is likely that the flow would be separated over the lower surface of a tailplane located in this position.

The wake skew angle and the asymmetry of the velocities in the wake increased as the advance ratio was increased. This is illustrated in Fig. 8, which shows the distribution of total pressure at an advance ratio of $\mu = 0.20$. The values of C_{p_0} at this higher advance ratio were much smaller, as expected (by definition C_{p_0} decreases with advance ratio for a given C_p). The low pressure region due to the hub increased signifi-

cantly in size and was convected further downstream, but still not close to the horizontal tailplane. The high total pressure region found at the rear of disk at low advance ratios moved towards the retreating side of the rotor, indicating that the loading on the retreating side had shifted more towards the blade tips.

Wake Geometry Measurements

Detailed positions of the rotor wake were determined from video images using the shadowgraph method. The shadowgraph images were analyzed to determine the position of the tip vortices, which identify the boundaries of the rotor wake. The wake boundaries for different test conditions are presented in Figs. 9–12. Each figure shows the location of the rear wake boundary along the longitudinal centerline for different advance ratios. The locations of the tail boom, vertical fin, and horizontal tailplane are also shown. The reference point for these figures is the center of the rotor hub rather than the origin of the TPP because the hub-plane is fixed with respect to the horizontal tailplane. Based on measured coning angles, the TPP was located approximately $0.050R$ above the hub-plane.

Figure 9 shows the baseline wake boundaries, which are for a shaft angle of $\alpha_s = -2°$, a blade loading coefficient of 0.075 and with the high tail position. Figures 10–12 illustrate the effect of changing the test parameters. From the measured boundaries, it was clear that varying the advance ratio had the most significant effect on the wake geometry. At the lowest advance ratio of $\mu = 0.05$, the tip vortices were initially convected down almost perpendicular to the TPP. As the vortices approached the body, however, they were convected almost parallel to the body surface. This process was observed during a previous test, and is discussed in detail in Refs. 26–28. An increase in advance ratio produced a higher wake skew angle, so the tip vortices were convected streamwise at a higher velocity. As expected, changes in the wake skew angle were largest at low advance ratios and as the advance ratio was increased the change in wake skew angle became smaller, the angle remaining almost constant above $\mu = 0.25$.

Due to the difficulty in obtaining high contrast video shadowgraphs at higher advance ratios, it was not always possible to follow the vortex filaments until they impacted on the empennage. However, the trajectories of the observed tip vortices were consistent enough to determine the position of the wake with respect to the horizontal tailplane. In those shadowgraph images where direct impingement of the wake on the vertical fin could be observed, the tip vortices were found to disintegrate quickly.

The effects on the wake geometry were found to be small after increasing the rotor colective pitch and blade loading coefficient to 0.085. Essentially, the tip vortices followed the same path as for the lower blade loading, and they appeared to be convected away from the rotor at nearly the same speed, despite the slight increase in mean inflow velocity corresponding to the thrust increase. However, the shadowgraph contrast was slightly improved due to the increase in tip vortex strength, allowing more of the wake to be observed at higher advance ratios.

Descent conditions in forward flight were simulated

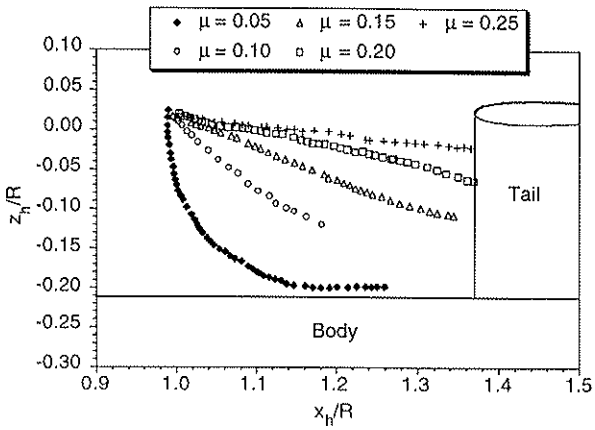

Figure 9: Wake boundaries for $\alpha_s = -2°$, $C_T/\sigma = 0.075$, and high tail position

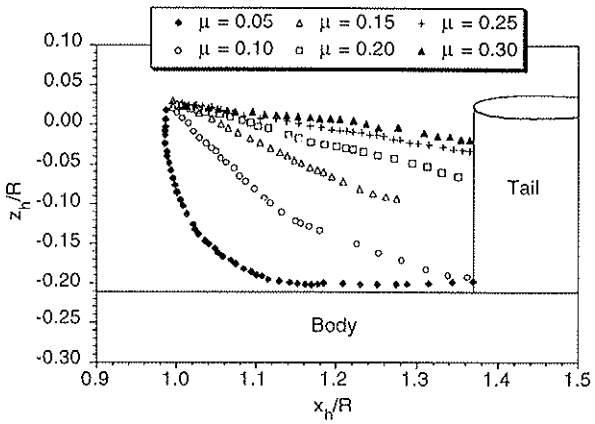

Figure 10: Wake boundaries for $\alpha_s = -2°$, $C_T/\sigma = 0.085$, and high tail position

by tilting the shaft axis back to $\alpha_s = +2°$. This resulted in a more substantial change to the wake boundaries, especially at high advance ratios. The wake boundary now passed very close to the horizontal tailplane for $\mu = 0.25$ and 0.30. The wake skew angle was almost constant at these advance ratios, and the observed wake boundaries were virtually identical.

Lowering the vertical position of the horizontal tailplane had little effect on the wake geometry for a given set of conditions, and the observed wake boundaries were essentially identical to those observed with the high tail. However, with the lower position the trailing-edge of the rotor wake now passed over the tailplane at $\mu = 0.25$ and impinged on the top surface. Such close interactions were not observed with negative shaft angles at the high tail position, where the wake passed below the horizontal tailplane for all advance ratios.

Time-Averaged Pressures

Time-averaged pressure measurements were made at thirty-two locations that were distributed spanwise along the leading- and trailing-edges of the horizontal tail. As suggested by the wake surveys, the flow about the horizontal tail was found to be inherently three-dimensional. This was previously shown by Leishman

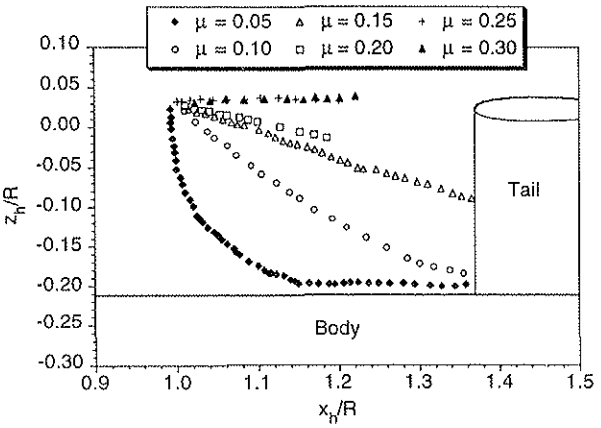

Figure 11: Wake boundaries for $\alpha_s = +2°$, $C_T/\sigma = 0.075$, and high tail position

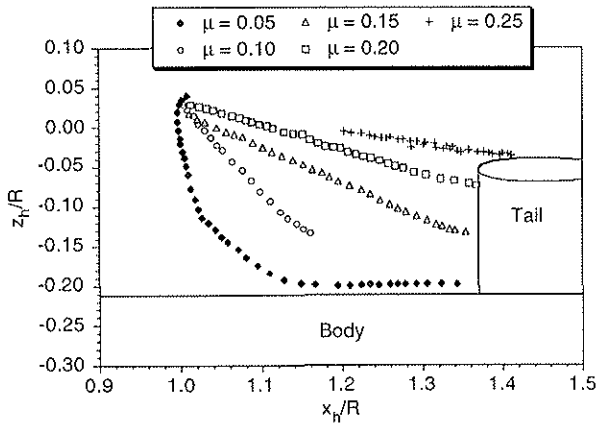

Figure 12: Wake boundaries for $\alpha_s = -2°$, $C_T/\sigma = 0.085$, and low tail position

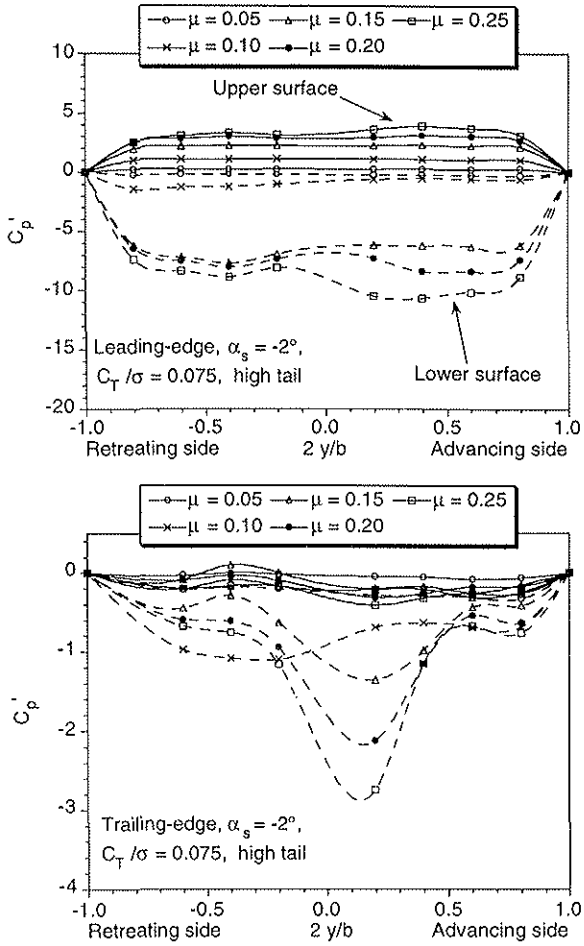

Figure 13: Spanwise steady pressure distributions for $\alpha_s = -2°$, $C_T/\sigma = 0.075$, and high tail position

and Bi,[12] who encountered a wide variation in pressure distributions along the span of a lifting surface located in a rotor wake. The three-dimensionality was expected to be as severe in the current test, especially since the horizontal tailplane was situated on top of a vertical fin. The vertical fin was expected to generate some lift due to the effective side-slip angles that were measured in the wake survey, thus contributing to the overall asymmetry of the flow over the horizontal tail.

Spanwise pressure distributions measured over the horizontal tail are illustrated in Figs. 13–16. These pressure distributions correspond to the same test conditions as for the wake geometries shown in Figs. 9–12. Each figure shows both the pressure distribution along the leading- and trailing-edges. The solid line represents pressures along the upper surface, and the dashed line represents pressures along the bottom surface. Since the horizontal tailplane was operating in a flow environment that was more dependent on the rotor than on the freestream, the measured pressures have been non-dimensionalized with respect to the rotor tip speed.

The pressure distributions over the tail showed generally positive (stagnation) values of C_p' on the upper surface, and negative (suction) values on the lower surface. There was a clear difference between the advancing (starboard) and retreating (port) side of the tailplane, especially on the lower surface, the pressures on the advancing side of the tailplane being slightly higher along the leading-edge. This suggested that the (negative) lift on the advancing side was larger as a result of the higher strength of the vortex bundle trailed from this side of the rotor. The asymmetry is also partly due to the physical separation by the vertical fin, which divided the flow over the tailplane at midspan.

Pressure distributions for a rotor shaft angle of $\alpha_s = -2°$ and the high tail position are shown in Fig. 13 ($C_T/\sigma = 0.075$) and Fig. 14 ($C_T/\sigma = 0.085$). These pressure distributions appeared qualitatively similar, although, as expected, the observed pressures were slightly larger at the higher blade loading.

At advance ratios below $\mu = 0.15$ the pressures along the leading-edge of the tailplane were low, but significant suction pressure still existed along the trailing-edge. This result confirms that the flow was indeed separated. The flowfield measurements and flow visualization discussed previously indicated that the downwash angles at these advance ratios were quite high, and it is likely that the tail was completely stalled at these operating conditions.

As the advance ratio was increased to $\mu = 0.15$, a significant increase in the leading-edge suction pressures was observed. At the same time, the pressures

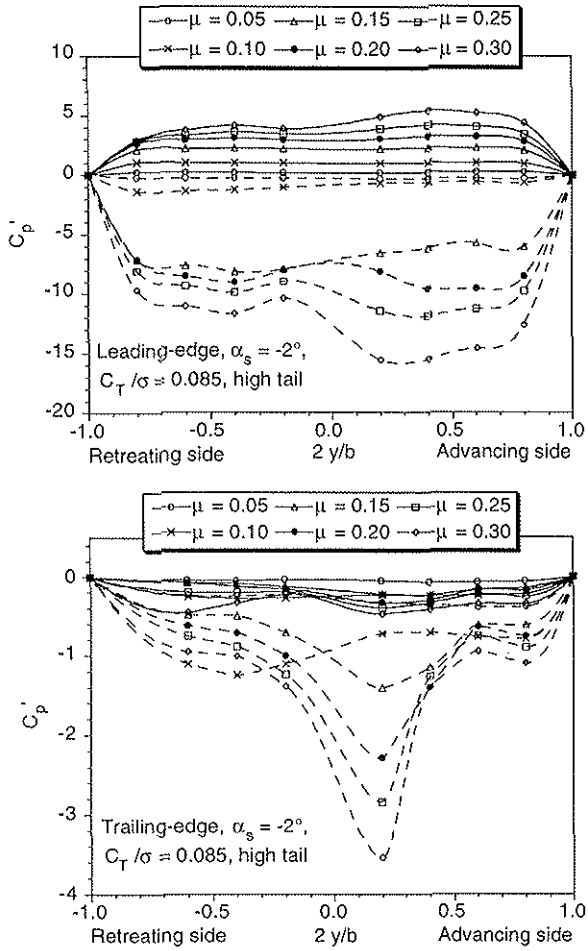

Figure 14: Spanwise steady pressure distributions for $\alpha_s = -2°$, $C_T/\sigma = 0.085$, and high tail position

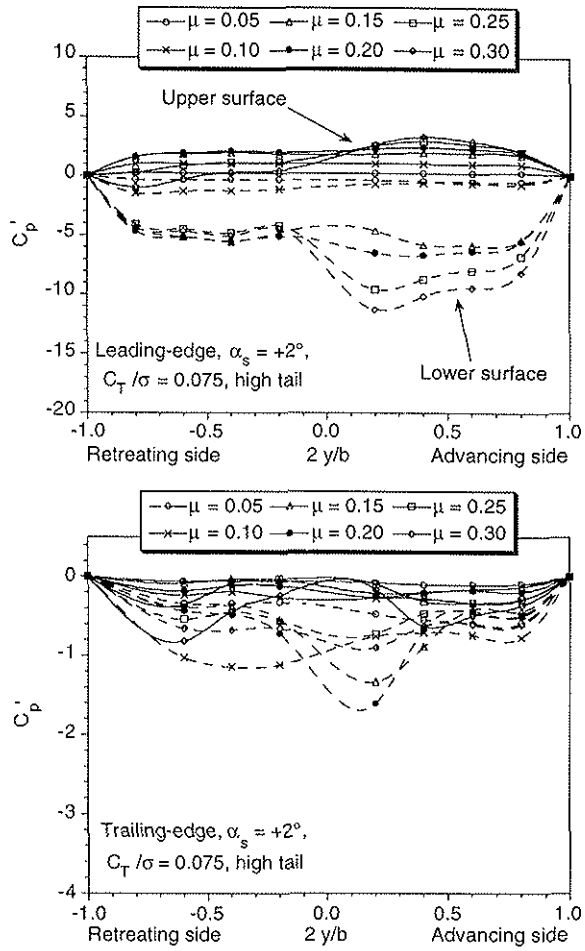

Figure 15: Spanwise steady pressure distributions for $\alpha_s = +2°$, $C_T/\sigma = 0.075$, and high tail position

along the trailing-edge decreased considerably, except at the measurement point just to starboard of the vertical fin. The flowfield survey and flow visualization has shown that the downwash angles decrease with advance ratio while the wake skew angle increased, so this resulted in a smaller angle of attack at the horizontal tailplane. It appears that the flow was now less separated but the tail was still operating at a high negative angle of attack.

At high advance ratios, a large suction peak appeared in the trailing-edge pressure distribution on the starboard (advancing) side of the tail. It is possible that there was a lateral flow towards the advancing side of the tailplane, such that the vertical fin was operating at a negative angle of attack. This was implied by the flowfield measurements of V_y (see Fig. 5), which showed that the lateral velocity was generally positive in the vicinity of the horizontal tail. This, combined with the magnitude of the trailing-edge suction peak, suggested that flow separation and a scarf vortex was likely present on the advancing side of the tailplane. This vortex originated at the junction of the vertical fin and the horizontal tailplane, and extended to the trailing-edge.

When the advance ratio was increased from $\mu = 0.15$ to 0.30, the pressure increases at the leading-edge of the lower surface were found to be much smaller. Recall that the pressures presented here have been non-dimensionalized with respect to the (constant) rotor tip speed, such that any increase in free-stream velocity affecting the horizontal tail results in an increase in C_p'. However, as the advance ratio increased, the downwash angles and corresponding angle of attack decreased, such that the net increase in C_p' was benign.

It is noteworthy that at $\mu = 0.15$, the leading-edge suction pressures on the bottom surface were slightly lower on the advancing side of the tail. This again indicated that the flow had just started to reattach here, while the flow on the retreating side was already fully attached. This can be explained through the asymmetry of the rotor wake. The stronger vortex bundle trailed on the advancing side led to higher downwash angles, delaying flow reattachment. As the advance ratio increased, the flow became fully attached and the unsteady pressure coefficient increased with the higher dynamic pressure. Therefore, the generally higher flow velocities on the advancing side led to higher suction pressures at the leading-edge of the tail.

Only mild changes to the tailplane pressure distributions was observed at low advance ratios when the rotor shaft angle was changed from $\alpha_s = -2°$ to $+2°$. This is because the tail was still fully stalled. Between

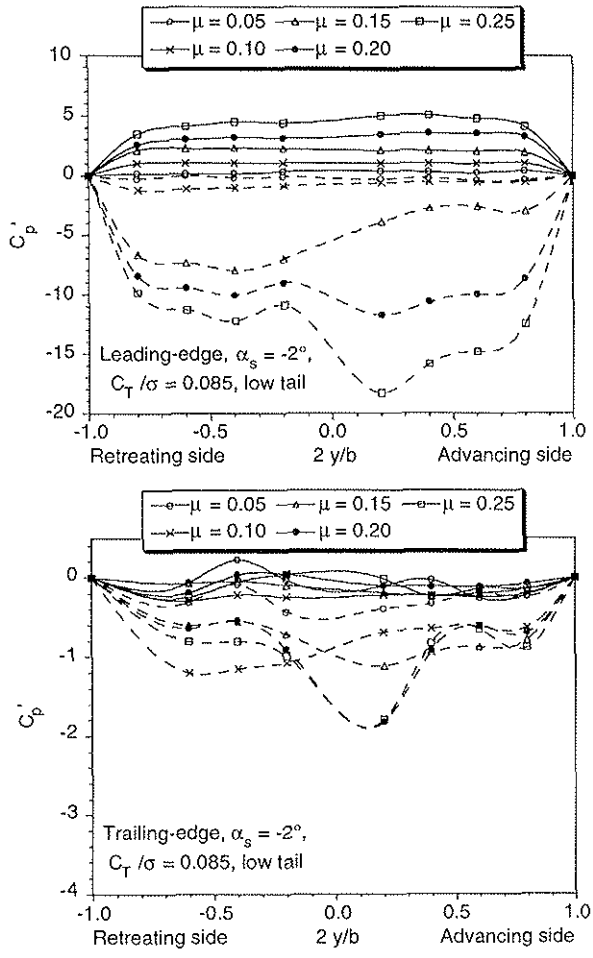

Figure 16: Spanwise steady pressure distributions for $\alpha_s = -2°$, $C_T/\sigma = 0.085$, and low tail position

$\mu = 0.15$ and 0.20, the flow became less separated and the pressure distributions looked similar to those for negative shaft angles. However, the leading-edge pressures were slightly smaller. This was expected because the observed wake skew angles were higher resulting in reduced angles of attack. The trailing-edge pressures showed a slight peak on the advancing side, indicating that the scarf vortex at the horizontal and vertical surfaces was still present.

As the advance ratio was increased to $\mu = 0.25$ the leading-edge pressures on the lower surface on the retreating side decreased, and suction pressures were observed on the upper surface suggesting that the retreating side of the tailplane was now operating at a very shallow angle of attack. Flow visualization of the same test conditions (see Fig. 11) confirmed this because the trailing-edge of the rotor wake boundary was convected almost parallel to the horizontal tailplane. On the advancing side of the tail the pressure peak at the trailing-edge disappeared, suggesting that the scarf vortex was no longer present. While the observed pressures here were low, no suction pressure was observed on the upper surface, thereby confirming that the tail was now operating at a small negative angle of attack.

Figure 16 illustrates the effects of lowering the tail position. Again, the flow about the tailplane was completely stalled at low advance ratios, and the flow on the retreating side was found to reattach at about $\mu = 0.15$. However, re-attachment on the advancing side of the tail did not occur until $\mu = 0.20$, suggesting that the asymmetry in the rotor wake was significantly higher for this tail position with higher downwash angles occurring on the advancing side.

As the advance ratio was increased to $\mu = 0.25$, high leading-edge suction pressures were measured. The wake geometry measurements (Fig. 12) showed that at this high advance ratio the wake was very close to the tailplane, and it is likely that the tailplane was encountering quite high local velocities, especially on the advancing side where the vortex bundle trailed from the disk was stronger. A small peak in the trailing-edge on the advancing side suggested that the scarf vortex was present at high advancing ratios, but it was not as intense as for the high tail position.

Unsteady Pressures

The time-dependent pressures measured on the tail showed more complex variations than were measured previously on the body surface.[2, 4] Also, it was not entirely possible to clearly classify the unsteady pressure signatures into categories, as was done in Ref. 1. This was not entirely unexpected, since the environment at the empennage location was much more three-dimensional due to the nature of the rotor wake and its roll-up as described previously, as well as the influence of the flow separation and wake system generated by the tail itself.

Like the time-averaged airloads, the general nature of the unsteady loads were found to be closely related to the proximity of the rotor wake boundary and, therefore, the blade tip vortices. For example, Fig. 17 shows representative time-dependent pressures measured at one location on the upper surface of the tailplane for a range of advance ratios at a constant rotor thrust and shaft angle for the low tail position. At low advance ratios ($\mu \leq 0.10$) the rotor wake was shown previously by the flow visualization results to convect relatively far below the tail, and the unsteady loads were found to be negligible. However, as the advance ratio was increased, the unsteady loads were found to quickly build in intensity. This is due to the closer proximity of the rotor wake boundary.

For the test conditions in Fig. 17, the wake boundary was very close to the tail between $\mu = 0.20$ and 0.25. This can be seen in Fig. 12, which represents nearly the same test conditions but with a slightly higher blade loading of 0.085. At this condition the unsteady loads reached their maximum value. For advance ratios above 0.25, the separation distance between the wake boundary and the horizontal tailplane increased slightly, with a corresponding mild decrease in unsteady loading. Recall that for high advance ratios the position of the wake boundary remains relatively unaffected by changes in advance ratio (see Figs. 10 and 11). Therefore, the unsteady loads were maintained at the same overall magnitude. However, since the convection velocity of the individual filaments increased with increasing advance ratio, a change in phase of the unsteady loads on the tail with respect to the blade position was still observed.

The effect of the horizontal tail position on the unsteady airloads can be more clearly illustrated by ex-

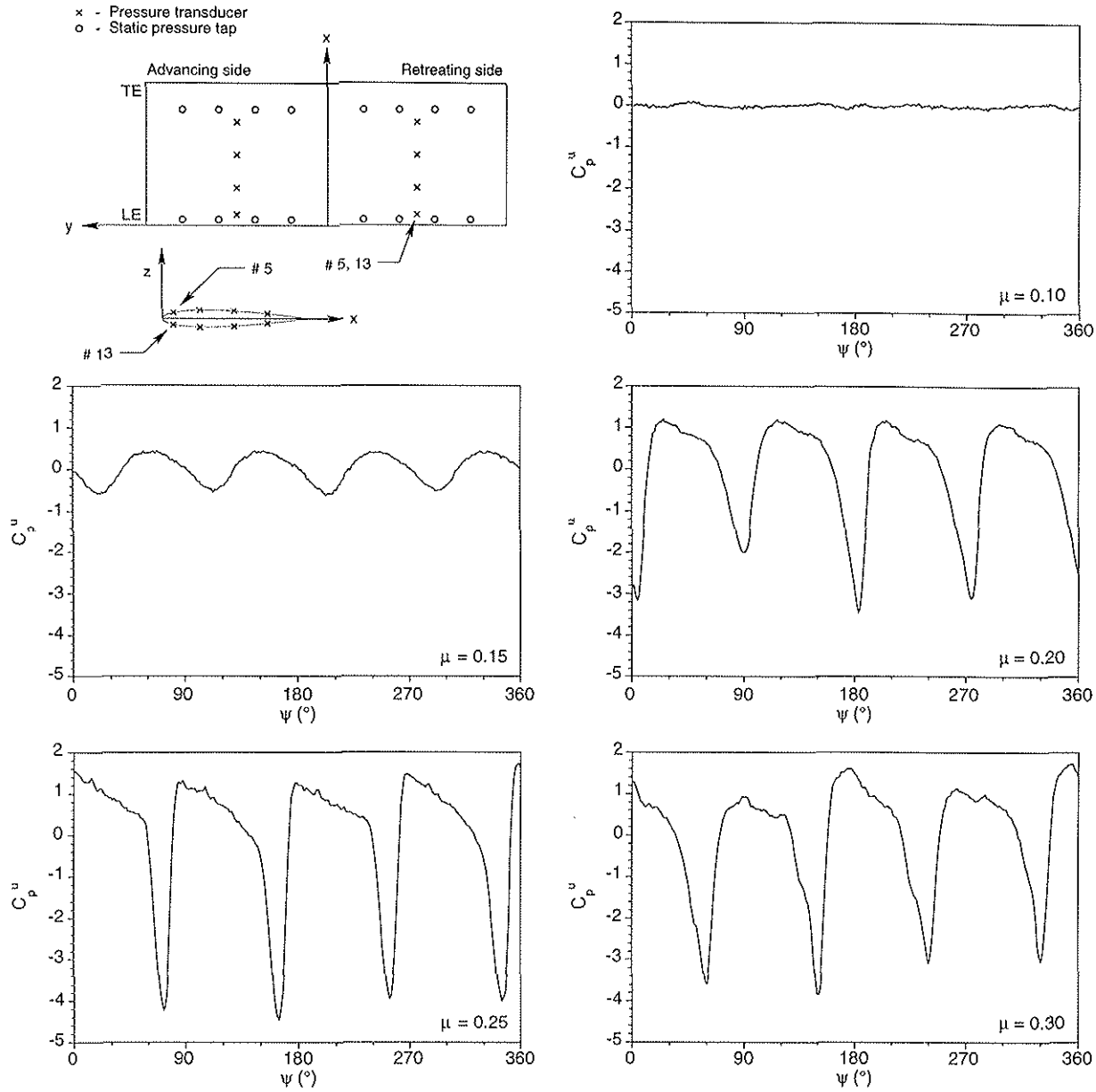

Figure 17: Variation of unsteady pressure coefficient with advance ratio at transducer # 5 (upper surface, retreating side, leading-edge) for $\alpha_s = -2°$, $C_T/\sigma = 0.075$, and low tail position

amination of the one-sided autospectral density function. This was obtained by computing the autocorrelation function of the time-history data, and subsequently performing an FFT. Figure 18 shows the variation in the 4 per-revolution ($4P$) and $8P$ loading with advance ratio for high and low tail configurations for blade loadings of $C_T/\sigma = 0.075$ and 0.085. These data are derived from measurements of the unsteady pressures at the leading-edge ($x/c = 0.075$) on the lower surface on the retreating side of the horizontal tail. The results correspond to the wake boundaries shown in Figs. 9, 10, and 12. The corresponding pressures on the upper surface of the tail are shown in Fig. 19.

For the high tail configuration the results showed a steady increase in unsteady airloading for both the $4P$ and $8P$ components. The primary cause for this was the decreasing separation distance between the wake boundary and the horizontal tailplane. A secondary cause was the increase in non-circulatory loading[15] because of the increase in streamwise wake convection velocity of the tip vortices. These trends were also obtained in a full-scale test discussed in Refs. 13 and 14. It is noteworthy that while the $4P$ forcing was the most dominant, significant $8P$ airloads were also present.

Below $\mu = 0.15$, both the $4P$ and $8P$ unsteady airloads were found to be quite small for both the low and high tail positions. This was expected since the wake boundary was relatively far from the tail at low advance ratios. Furthermore, as described previously, the time-averaged pressure measurements have shown that the flow over the tailplane was stalled below $\mu = 0.15$.

The variation in unsteady loading obtained with the low tail configuration was found to be considerably

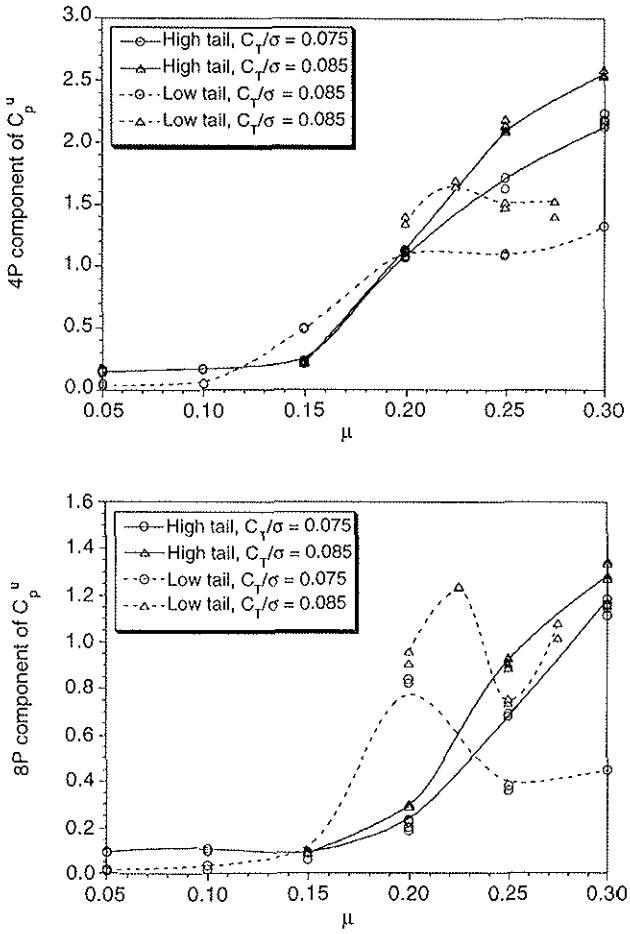

Figure 18: Variation of periodic pressures with advance ratio at transducer 13 for $\alpha_s = -2°$, and $C_T/\sigma = 0.075$

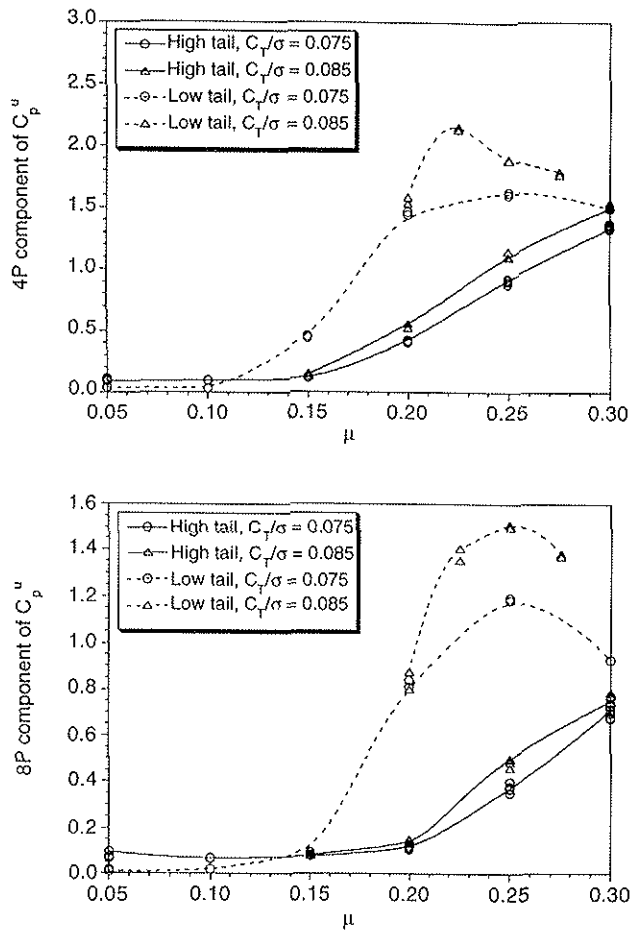

Figure 19: Variation of periodic pressures with advance ratio at transducer 5 for $\alpha_s = -2°$, and $C_T/\sigma = 0.075$

different to that obtained for the high tail. The $4P$ airloads began to increase at an advance ratio of only 0.10, which was because of the lower wake/tail separation distance. At an advance ratio of $\mu = 0.20$, as the wake boundary started to encroach on the horizontal tail, the $4P$ components reached approximately the same intensity as for the high tail configuration. However, a sharp increase in $8P$ airloads was also noticed here.

As the advance ratio was increased to 0.25, the tip vortices passed over the horizontal tailplane (see Fig. 12), and a very slight reduction in the $4P$ airloads was observed on the lower surface. More noticeable was the sharp decrease in $8P$ airloads when the wake boundary no longer impinged on the leading-edge of the tail surface.

Further increases of the advance ratio resulted in increases of both $4P$ and $8P$ airloads, which again was primarily due to the increase in the rotor wake convection velocity. It is noteworthy that the magnitude of the unsteady pressures for the low tail configuration was considerably smaller than for the high tail configuration.

Figure 19 illustrates the development of the $4P$ and $8P$ airloads on the upper surface of the horizontal tailplane. These airloads were measured at the leading-edge ($x/c = 0.075$) on the retreating side of the tail. For the high tail position, the $4P$ and $8P$ components were negligible below $\mu = 0.15$. However, as the advance ratio was increased, the unsteady loads were found to increase steadily, as had been observed on the lower surface of the tail. Yet the magnitude of the unsteady pressures was nearly 40% smaller than on the lower surface. The primary cause for this difference was separation from the wake. At the high tail position, the wake passed below the tail for all test conditions. Therefore, it was expected that the unsteady pressure response on the upper surface would be substantially lower than on the lower surface.

When the tail position was lowered, the magnitude of the unsteady pressures were found to increase sharply. As was observed on the lower surface of the tailplane, there was a significant increase in $8P$ loading when the wake impinged on the tail, while the $4P$ loading increased slightly. As the advance ratio was increased further and the vortices were convected further away from the tail, both the $4P$ and $8P$ airloads decreased. The maximum unsteady airloading occurred at a slightly higher advance ratio than on the lower surface because the wake impinged on the upper surface at a slightly higher wake skew angle.

The quantative behavior of the $4P$ and $8P$ airloads did not substantially change with blade loading. The increase in blade loading from $C_T/\sigma = 0.075$ to 0.085 produced higher inflow velocities, resulting in a slightly lower wake skew angle. This meant that the

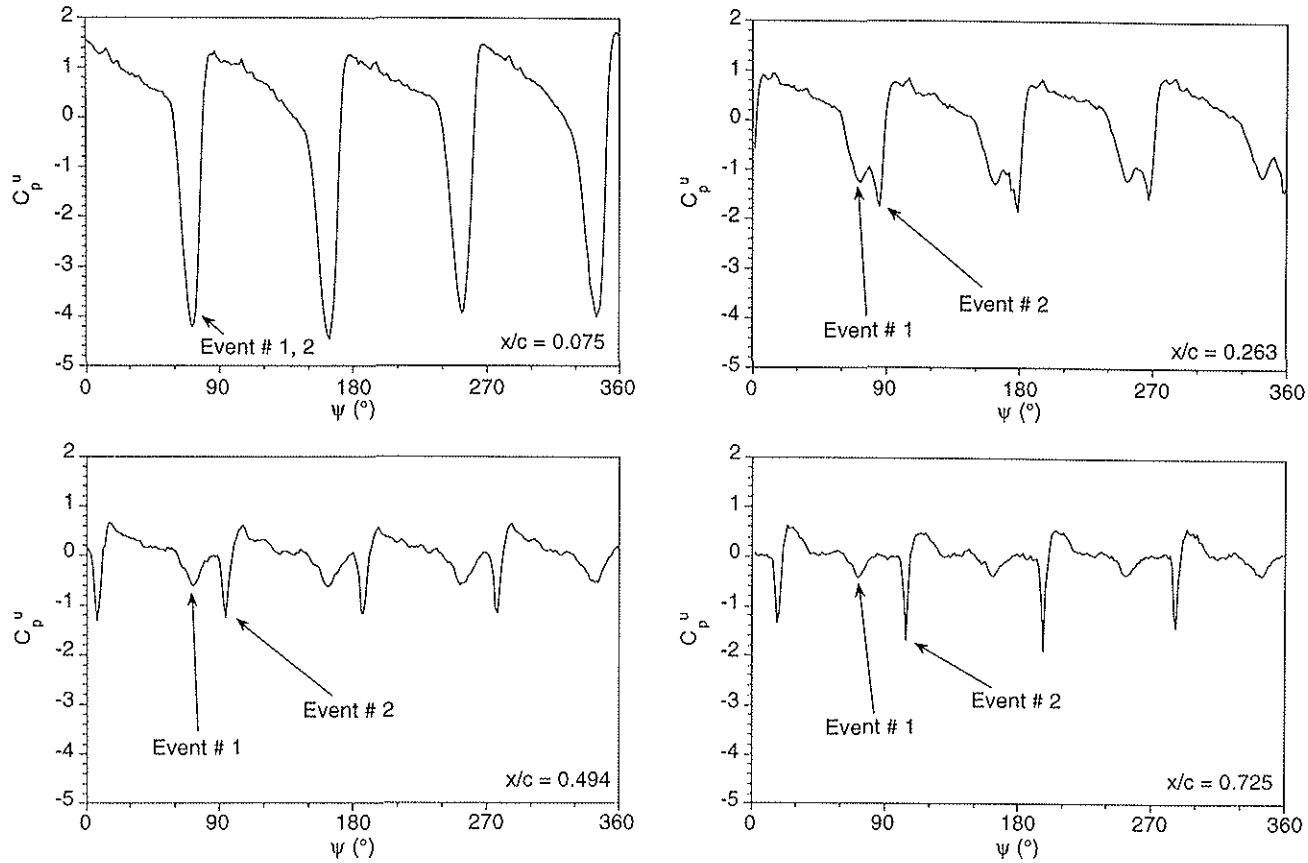

Figure 20: Variation of unsteady pressure coefficient with chordwise position on the retreating side of the upper surface for $\mu = 0.25$, $\alpha_s = -2°$, $C_T/\sigma = 0.075$, and low tail position

wake impinged on the tailplane at a higher advance ratio, which was shown by a corresponding shift in the $8P$ pressure peak. Furthermore, the increased blade loading produced slightly higher tip vortex strengths, also resulting in a higher $4P$ and $8P$ airloading.

Note that the time-varying induced velocity field produced by the convecting tip vortices resulted in local time-varying angles of attack at a fairly high reduced frequency. This can be established by computing the reduced frequency at the tailplane from the equation

$$k = \frac{\omega c}{2V} \approx \frac{(N_b\Omega)(c/R)R}{2\mu\Omega R} = \frac{N_b(c/R)}{2\mu}$$

The ratio c/R is about 0.25 for the present configuration, so the reduced frequency of the flow at the tail for an advance ratio of 0.2 would be of order 2.5. Obviously this requires the mathematical modeling of the problem to be considered fully unsteady. Also, if and when stall occurs locally on the wing, the high effective reduced frequency of the flow means that separation and stall may be more dynamic in nature. This adds an additional level of complexity to the mathematical modeling of the rotor/empennage interaction problem.

Figure 20 shows measured time-dependent pressures at different chordwise positions on the upper surface of the retreating side the tail. Moving chordwise, the magnitude of the unsteady loads was found to diminish quickly. This is analogous to the steady state pressure distribution on a lifting surface, where the largest variations in pressure are observed near the leading-edge. Furthermore, the interaction with the lifting surface itself may alter the strengths and/or structure of the tip vortices in the wake, also resulting in a reduced magnitude of unsteady loading.

From Fig. 20, it appeared that the unsteady loading consisted of a superposition of two events. The first event was evidenced by a large increase in suction pressure observed near the leading-edge ($x/c = 0.075$) at $\psi = 71°$. The magnitude of this change in pressure decreased quickly along the chord, and it was barely visible at $\psi = 73°$ at $x/c = 0.263$. Only a slight change in phase was observed between different chordwise measurement points, suggesting that the pressure disturbance is due to unsteady lift generation on the tail due to the induced velocity field. The second event was much more consistent in magnitude, and is visible at $\psi = 86°$ at $x/c = 0.263$, at $\psi = 93°$ at $x/c = 0.494$, and at $\psi = 104°$ at $x/c = 0.725$. This event was characterized by a very sharp decrease in pressure, followed by a sharp increase. There was a significant chordwise phase lag in the measurements of this event, suggesting that the disturbance was being convected past the tail at the local flow velocity. The general overall pressure signature due to the second event was typical of vortex passage, and corresponded well with the signature of close vortex/surface interactions observed by Bi and Leishman.[1]

The measured time-dependent pressures at different locations on the upper and lower surface showed the same overall types of signatures, but they were

quite varied in magnitude and phase. In general, the observed sensitivity of the pressure loads at different points on the wing will make the theoretical prediction of these effects a significant challenge to the analyst.

Summary and Conclusions

An experimental investigation has been conducted to study the aerodynamic interactions between a helicopter rotor and a T-tail empennage in forward flight. The following conclusions were drawn from the investigation:

1. Velocity field measurements showed that the flow below and behind the rotor was highly asymmetric. The individual tip vortices generated by the rotor blades were found to roll-up quickly behind the rotor disk to form two vortex bundles. These vortex bundles were the dominant feature in the flow behind the rotor disk, and greatly affected the vertical and horizontal velocity components induced at the tail location.

2. The measured location of the rotor wake boundary showed that at low advance ratios the rear of the rotor wake impinged on the tail of the body and had little effect on the horizontal tailplane. As the advance ratio was increased the wake skew angle increased and the wake was observed to impinge on the vertical tail and finally the horizontal tail. For some conditions, the wake passed over the top of the horizontal tail. At high advance ratios, the wake skew angle remained nearly constant with the tip vortices being convected downstream almost parallel to the rotor tip-path-plane.

3. At low advance ratios the tail encountered high downwash angles and the flow over the horizontal tail was generally stalled. However, the flow progressively reattached over the tail as the advance ratio was increased. The time-averaged airloading was asymmetric due, primarily, to the difference in strength of the wake vortex bundles trailed from the sides of the rotor disk. Under some test conditions, a sharp trailing-edge pressure peak was observed on the retreating side of the horizontal tail, perhaps indicating that a scarf vortex originated at the junction of the vertical fin and the horizontal tail.

4. Time-varying pressures showed that flowfield near the horizontal tailplane was highly unsteady and very dependent on the position of the rotor wake boundary, the tip vortex strengths, and their convection velocity. Below an advance ratio of 0.15 the unsteady pressure responses were generally small because the rotor wake was far from the tailplane. As the advance ratio was increased the wake boundary encroached on the tailplane, and the unsteady pressures increased significantly in magnitude. When the wake impinged on the tail, a sharp increase in the $8P$ component of unsteady pressure was observed.

5. The unsteady pressure responses over the horizontal tail appeared to be characterized by two events. The first, and more dominant, was due to the unsteady lift produced on the horizontal tail that was induced by rotor wake. This part of the unsteady pressure response was mostly in-phase at all points over the chord. The second event, which was smaller in magnitude, was due to the disturbances produced by the convection of the individual tip vortices past the measurement points. These pressures were out-of-phase over the chord.

Acknowledgments

This work was partly supported by the U.S. Army Research Office under contract DAAH-04-93-G-001. The authors wish to thank Dhananjay Samak, Naipei Bi, David Platz, Ashish Bagai, and the staff of the Glenn L. Martin wind tunnel for their assistance in the tests.

References

[1]Bi, N., and Leishman, J. G., "Experimental Study of Aerodynamic Interactions Between a Rotor and Fuselage," AIAA 7th Applied Aerodynamics Conference, Seattle, WA, July-August 1989. Also in *Journal of Aircraft*, Vol. 27, (9), September 1990.

[2]Leishman, J. G., and Bi, N., "Aerodynamic Interactions between a Rotor and a Fuselage in Forward Flight," American Helicopter Society 45th Annual Forum, Boston, MA, May 1989.

[3]Leishman, J. G., and Bi, N., "Investigation of Aerodynamic Interactions between a Rotor and Fuselage in Forward Flight," *Journal of the American Helicopter Society*, Vol. 35, (3), July 1990.

[4]Crouse, G. L., Leishman, J. G., and Bi, N., "Theoretical and Experimental Study of Unsteady Rotor/Body Aerodynamic Interactions," *Journal of the American Helicopter Society*, Vol. 37, (1), January 1992.

[5]Prouty, R. W., "Development of the Empennage Configuration of YAH-64 Advanced Attack Helicopters," USAAVRADCOM-TR-82-D-22, February 1983.

[6]Main, B. J., and Mussi, F., "EH-101 — Development Status Report," 16th European Rotorcraft Forum, Glasgow, Scotland, September 1990.

[7]Wheatley, J. B., "The Influence of Wing Setting on the Wing Load and Rotor Speed of a PCA-2 Autogiro as Determined in Flight," NACA Rep. 536, 1935.

[8]Makofski, R. A., and Menkick, G. F., "Investigation of Vertical Drag - Periodic Loads Acting on Flat Panels in a Rotor Slipstream," NACA TN 3900, December 1956.

[9]McKee, J. W., and Naeseth, R. L., "Experimental Investigation of the Drag on Flat Plates and Cylinders in the Slipstream of a Hovering Rotor," NACA TN 4239, April 1958.

[10]Lynn, R. R., "Wing-Rotor Interactions," *Journal of Aircraft*, Vol. 3, (4), July-August 1966.

[11]Sheridan, P. F., and Smith, R. P., "Interactional Aerodynamics — A New Challenge to Helicopter Technology," American Helicopter Society 35th Annual Forum, Washington, DC, May 1979.

[12]Leishman, J. G., and Bi, N., "Experimental Investigation of Rotor/Lifting Surface Interactions," *Journal of Aircraft*, Vol. 31, (4), July–August 1994.

[13]Torok, M. S., and Ream, D. T., "Investigation of Empennage Airloads Induced by a Helicopter Main Rotor Wake," American Helicopter Society 49th Annual Forum, St. Louis, MO, May 1993.

[14]Frederickson, K. C., and Lamb, J. R., "Experimental Investigation of Main Rotor Wake Induced Vibratory Empennage Airloads for the RAH-66 Comanche Helicopter," American Helicopter Society 49th Annual Forum, St. Louis, MO, May 1993.

[15]Bramwell, A. R. S., "A Theory of the Aerodynamic Interference Between a Helicopter Rotor Blade and a Fuselage and Wing in Forward Flight," *Journal of Sound and Vibration*, Vol. 3, (3), May 1966.

[16]Gangwani, S. T., "A Doublet-Lattice Method for the Determination of Rotor Induced Empennage Vibration Airloads — Analysis, Description, and Program Documentation," NASA CR-165893, June 1982.

[17]Gangwani, S. T., "Calculation of Rotor Wake Induced Empennage Airloads," *Journal of the American Helicopter Society*, Vol. 29, (2), April 1983.

[18]Mello, O. A. F., and Rand, O., 11 Unsteady Frequency Domain Analysis of Helicopter Non-Rotating Lifting Surfaces," *Journal of the American Helicopter Society*, Vol. 36, (2), April 1991.

[19]Curtiss, H. C., and Quackenbush, T. R., "The Influence of the Rotor Wake on Rotorcraft Stability and Control," 15th European Rotorcraft Forum, Amsterdam, The Netherlands, September 1989.

[20]Weinstock, S., "Formulation of a Simplified Model of Rotor-Horizontal tailplane Interactions and Comparison with Experimental Measurements," 17th European Rotorcraft Forum, Berlin, Germany, September 1991.

[21]Leishman, J. G., and Bi, N., "Experimental Data on the Aerodynamic Interactions Between a Helicopter Rotor and an Airframe," AGARD-AR-303, Vol. II, August 1994.

[22]Leishman, J. G., and Bi, N., "Measurements of a Rotor Flowfield and the Effects of a Fuselage in Forward Flight," *Vertica*, Vol. 14, (3), 1990.

[23]Bagai, A., and Leishman, J. G., "Improved Wide-Field Shadowgraph Set-up for Rotor Wake Visualization," *Journal of the American Helicopter Society*, Vol. 37, (3), July 1992.

[24]Roesch, P., and Dequin, A. M., "Experimental Research on Helicopter Fuselage and Rotor Hub Wake Turbulence," *Journal of the American Helicopter Society*, Vol. 32, (1), January 1985.

[25]Ghee, T. A., and Elliott, J. W., "The Wake of a Small-Scale Rotor in Forward Flight Using Flow Visualization," *Journal of the American Helicopter Society*, Vol. 40, (3), July 1995.

[26]Leishman, J. G., and Bagai, A., "Fundamental Studies of Rotor Wakes in Low Speed Forward Flight Using Wide-Field Shadowgraphy," AIAA Paper 91-3232, AIAA 9th Applied Aerodynamics Meeting, Baltimore, MD, September 1991.

[27]Bagai, A., and Leishman, J. G., "Experimental Study of Rotor Wake/Body Interactions in Hover," *Journal of the American Helicopter Society*, Vol. 37, (4), October 1992.

[28]Moedersheim, E., Daghir, M., and Leishman, J. G., "Flow Visualization of Rotor Wakes Using Shadowgraph and Schlieren Techniques," Paper 31, 20th European Rotorcraft Forum, Amsterdam, The Netherlands, October 1994.